MODELLING THE BEHAVIOR OF I-SHAPE CONCRETE BEAMS REINFORCED WITH FIBERS AND PRESTRESSED STEEL AND GFRP BARS

KAMYAR B. SHAHRBIJARI[*†], JOAQUIM A. O. BARROS[*††], ISABEL VALENTE[*††], GINTARIS KAKLAUSKAS[††††]

[*]ISISE, Dep. Civil Engineering, University of Minho
Guimarães, Portugal
e-mail: [†]kamyar.ba@civil.uminho.pt, [††]barros@civil.uminho.pt, [†††]isabelv@civil.uminho.pt

[††††]Dep. RC Structures and Geotechnics, Vilnius Gediminas T University
Vilnius, Lithuania
e-mail: gintaris.kaklauskas@vilniustech.lt

Key words: Hybrid flexural reinforcement, Fiber reinforced concrete beams, Nonlinear finite element analysis

Abstract: This paper reports the behavior of I-shaped fiber reinforced concrete (FRC) beams flexurally reinforced with prestressed steel and glass fiber reinforced polymer (GFRP) bars. The use of steel fibers aims to enhance the durability of pre-fabricated concrete structures by partially or completely replacing steel stirrups. In addition, GFRP and steel bars/tendons are combined as flexural reinforcement, creating a hybrid reinforcement system. GFRP bars are immune to corrosion and are positioned with minimum concrete cover, while steel reinforcement has adequate concrete cover thickness to minimize its risk to corrosion and ensure the required flexural capacity in a fire occurrence. Nonlinear finite element analysis (NLFEA) software was utilized for a critical analysis on the use of smeared crack model for predicting the behavior of this type of beams, including deflection, crack pattern, load-carrying capacity, and failure modes.

1 INTRODUCTION

In recent years, fiber reinforced concrete (FRC) has gained significant attention as a sustainable and reliable construction material due to its enhanced mechanical properties and durability. The incorporation of short fibers can effectively improve the brittle failure of concrete and control crack development [1, 2]. Additionally, the use of glass fiber-reinforced polymers (GFRP) as a total or partial replacement of traditional steel bars has become a growing trend in the field of structural engineering, mainly due to the vulnerability of traditional steel reinforcement to corrosion [3]. GFRP bars possess excellent corrosion resistance, but beams reinforced solely with GFRP bars tend to exhibit brittle failure modes [4, 5]. Additionally, GFRP bars have strong decrease of their mechanical properties under relatively high temperatures [6]. To enhance the ductility of GFRP-reinforced beams, a hybrid reinforcement composed by , steel and GFRP bars has been proposed [7].

When considering the shear capacity of reinforced concrete (RC) elements, the utilization of GFRP bars as flexural reinforcement can have adverse consequences on the dowel effect and aggregate interlock shear resisting mechanisms. This is due to their lower axial and shear stiffness, which permits larger openings and sliding of the critical diagonal cracks [8, 9].

The steel flexural reinforcement ratio should be determined to ensure a ductile failure mode in case of fire occurrence. If the flexural reinforcement is applied with a certain prestress, the beam's load-carrying capacity of at service-limit state (SLS) conditions can increase [10], as well its shear capacity [11].

Nonlinear finite element analysis (NLFEA) is a powerful strategy for predicting the behavior of RC beams under SLS and ultimate limit state (ULS) conditions. NLFEA has been widely used to investigate the behavior of FRC beams flexurally reinforced with prestressed steel and GFRP bars [12].

Mustafa et. al. (2018) [13] performed NLFEA to investigate the behavior of concrete beams flexurally reinforced with GFRP/CFRP and steel bars, observing the steel reinforcement in hybrid GFRP/steel reinforced concrete beams enhances the ductility and load resistance of the beams after cracking.

Soltanzadeh et. al. (2016) [14] utilized a FEM-based computer program with a plastic-damage multidirectional fixed smeared crack model to accurately predict the behavior of steel fiber reinforced self-compacting concrete (SFRSCC) beams flexurally reinforced with steel and GFRP bars. The concluded that, by prestressing this flexural reinforcement, the shear capacity of the SFRSCC beams was significantly increased.

By simulating concrete beams, without any type of shear reinforcement, and flexurally reinforced with GFRP bars, Barros et. al. (2021) [15] demonstrated that a multi-directional fixed smeared crack model (MDFSCM) can accurately predict the relevant behavioral features of this type of structural element, as long as a crack shear softening law is used.

Despite the developments that have been made on smeared and discrete crack models (SCM, DCM [18, 19]), recent blind simulation competitions on the use of these approaches demonstrate their fragilities, mainly in elements failing in shear and on the verifications for SLS conditions [16, 17], specially the SCM.

The level of accuracy of SCM for predicting the behaviour of elements failing in shear is quite dependent on the type of approach that simulates the crack shear stress transference [18]. The use of a shear retention factor [19] or a crack shear softening diagram [20] are the most current approaches for simulating the crack shear stress transfer, but the determination of reliable data for their definition is still a challenge, mainly in the case of a shear softening diagram.

The FEMIX computer program incorporates a MDFSCM [15], which allows for the consideration of shear retention concepts, including constant values or dependence on crack opening, as well as the use of crack shear softening diagrams.

In this study, the capabilities and limitations of the MDFSCM in modeling the behavior of hybrid FRC beams failing in shear are evaluated through an experimental program conducted by Mazaheripour et. al. [21]. This study focused on simply supported SFRC beams without stirrups and flexurally reinforced by hybrid prestressed GFRP-steel rebars. Regarding the numerical simulations, the following aspects were analyzed: the influence of finite element mesh refinement on the obtained results; the bond conditions between the GFRP flexural reinforcement and the surrounding concrete; the dispersion of the fracture mode I parameters registered experimentally, on the numerical predictions; the influence on using a shear retention factor over a crack shear softening diagram on the predictive performance.

2 EXPERIMENTAL PROGRAM

Figure 1 illustrates the geometric properties, reinforcement details, support, and loading conditions of the beams of the experimental program conducted by Mazaheripour et. al. [21]. Four I-shaped beams, namely IB5, IB6, IB8, and IB10, were selected from the experimental tests, each with equal reinforcement but varying the level of prestress in the hybrid flexural reinforcement. The geometry, reinforcement arrangements,

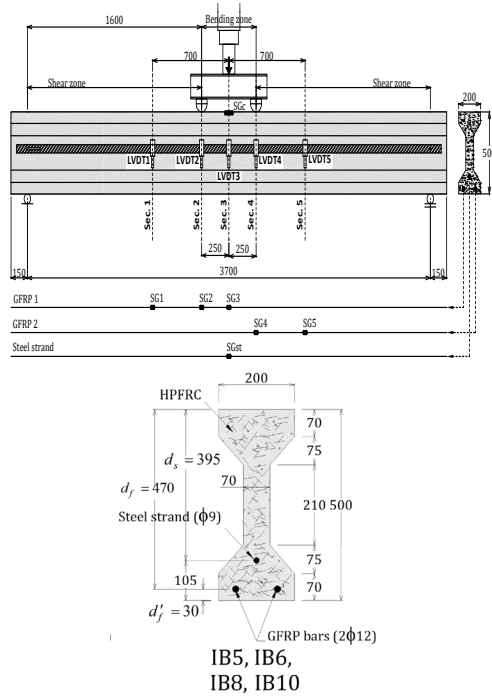support and loading conditions of these beams are illustrated in Figure 1.

Figure 1: Geometry, reinforcement details, and support and loading conditions of the beams of the test program (dimensions in mm) (adapted from [21]).

Each beam was flexurally reinforced with two GFRP bars of 12 mm diameter and a total cross-sectional area of 269 mm² , as well as one steel strand of 9 mm diameter and a cross-sectional area of 51.6 mm². Table 1 provides the nominal mechanical properties of the reinforcements used in the selected beams determined based on information provided by the manufacturers.

Beam IB5 had no prestress applied to either the GFRP bars or the steel strand, being considered the reference beam. The GFRP bars and steel strand of IB6, IB8 and IB10 beams were prestressed. The prestress in the steel strand (f_s^{pre}) was 800 MPa in all beams, while a prestress of 200 MPa, 400 MPa, and 540 MPa was applied in the GFRP bars (f_f^{pre}) of IB6, IB8, and IB10 beams, respectively, see Table 2. The average pre-strain losses at the time of testing were approximately 13.6% for GFRP bars and 9.8% for the steel strand, compared to the pre-strain measured on the day of prestressing these reinforcements.

Table 1: Nominal properties of the GFRP rebars and steel tendons used in the present study.

Type	Diameter	Cross section area	Modulus of elasticity	Yielding strain	Yielding stress	Ultimate stress	Ultimate strain	Weight
	ϕ_f , ϕ_s	A_f , A_s	E_f , E_s	ε_{sy}	f_{sy}	$f_{fu} f_{su}$	$\varepsilon_{fu} , \varepsilon_{su}$	
	(mm)	(mm²)	(GPa)	(%)	(MPa)	(MPa)	(%)	(g/m)
GFRP bar	13.1	134.5	60.0	–	–	1350	2.25	317
Steel strand	9	51.6	187.5	~0.8	~1600	~1900	>3.5	405

Table 2 Beam identification, reinforcing ratio of GFRP and steel bars, prestress level, maximum load, its central deflection, and failure mode.

Beam ID	ρ_f	ρ_s	f_s^{pre}	Prestress level (Steel)	f_f^{pre}	Prestress level (GFRP)	$M_{u,exp}$	P_{max}	Deflection at P_{max}	ε_f^*	ε_s^*	Mode of failure
	(%)	(%)	(MPa)	(%)	(MPa)	(%)	(MPa)	(kN)	(mm)	(%)	(%)	
IB5	0.29	0.07	0.0	0	0	0	148	185	47	1.05	-	Shear
IB6	0.29	0.07	800	50	200	15	186	232	64	1.09	-	Flexo shear
IB8	0.29	0.07	800	50	400	30	201	251	70	2.13	1.17	Flexo shear
IB10	0.29	0.07	800	50	540	40	210	262	70	2.12	-	Flexo shear

* The last value of strain recorded during the monotonic test

The SFRSCC with 90 kg/m^3 of steel fibers was prepared following the mixing method described elsewhere [22]. The concrete incorporated hooked-end steel fibers with a length of 33 mm, an aspect ratio of 65, and a yield stress of 1100 MPa.

To evaluate the compressive strength and Young's modulus of the SFRSCC, 25-cylinder specimens with a diameter of 150 mm and a height of 300 mm were subjected to compression tests according to ASTMC39 standards [23]. It was obtained an average compressive strength of 73 MPa with a coefficient of variation (CoV) of 6%, and an average Young's modulus of 35.4 GPa with a CoV of 3%.

The average residual flexural tensile strength parameters of the SFRSCC ($f_{R,i}$, i=1 to 4) were obtained from the applied force (F) versus the Crack Mouth Opening Displacement (*CMOD*) diagrams [24] by executing three point notched beam bending tests according to the recommendations of EN 1465 [25]. Two distinct sets of notched beams were examined, with each group consisting of 5 specimens. The first set comprised standard specimens measuring 150×150×600mm, featuring a notch depth of 35 mm. The second set involved testing notched beam specimens derived from intact sections at both ends of the beams, with dimensions of 70×70×600mm and a notch depth of 15 mm. The obtained results are presented in Table 3.

Table 3: The residual flexural tensile strength parameters of SFRSCC

	Residual flexural tensile strength parameters							
	$CMOD_1$		$CMOD_2$		$CMOD_3$		$CMOD_4$	
	F_1	$f_{R,1}$	F_2	$f_{R,2}$	F_3	$f_{R,3}$	F_4	$f_{R,4}$
	(kN)	(MPa)	(kN)	(MPa)	(kN)	(MPa)	(kN)	(MPa)
Average of first series (150x150x600mm)	30.65	11.59	30.81	11.65	28.25	10.68	25.26	9.55
Average of second series (70x70x600mm)	2.37	8.37	2.47	8.73	2.25	7.99	2.06	7.511

The I shape beams were subjected to a four-point bending test configuration until failure, utilizing a servo-hydraulic actuator under monotonic loading conditions with 500 mm between the loads (Figure 1). The actuator's piston was displacement-controlled, with a speed of 0.01 mm/s. However, for beam IB10, the monotonic behavior was examined after it has been subjected to two million fatigue loading cycles.

The experimental results reveal a trend for an increase of the beam's shear capacity with the prestress level applied to the flexural reinforcement, which is attributed to the favorable mechanism of aggregate interlock and higher uncracked SFRC area. A comparison between the experimental results of different beams also reveals that increasing the prestress level in GFRP bars leads to an enhancement in the load-carrying capacity.

This trend was also evident in the deflection of the beams. In cases where prestress was applied, a plateau in load deflection was observed after reaching a deflection of 35mm, indicating no further increase in the load. Moreover, an elevation in the prestress level corresponded to an increase in the strain experienced by GFRP bars at failure.

3 NUMERICAL MODEL AND SIMULATIONS

This chapter presents the modeling strategies employed to critically evaluate the potential of the MDFSCM in predicting the behavior of RC beams presented in the previous section. The simulations were carried out with a MDFSCM available in FEMIX computer program, whose details are described elsewhere [26].

3.1 Numerical model

3.1.1 Simulation of FRC

According to the MDFSCM, a crack (in reality, cracks are smeared in the corresponding integration point (IP)) is formed when the principal tensile stress, σ_I, attaints the tensile strength of the material (f_t) at less than an adopted small tolerance. A new crack is formed in an already cracked IP when besides the previous criterium, the angle formed between the new crack and previous active cracks (not completely closed) is higher than an adopted threshold angle (in general $\theta_{th} \in$ [30-60]°). For avoiding numerical instabilities with the occurrence of several crack status changes during the loading process, a maximum number of cracks ($N_{\max}^{cr}$) of 3 and 4 is generally adopted for, respectively, 2D and 3D type MDFSCM.

In the context of a structure subjected to 2D plane stress state, such is the present case, the constitutive law that governs the opening and sliding of a crack is:

$$\underline{D}^{cr} = \begin{bmatrix} D_n^{cr} & 0 \\ 0 & D_s^{cr} \end{bmatrix} \tag{1}$$

where D_n^{cr} and D_s^{cr} represent, respectively, the fracture mode I (in n direction, orthogonal to the crack plane) and mode II (in s sliding direction), Figure 2.

w : crack opening
δ : crack sliding
σ_{ct}^{cr} : crack normal tensile stress
τ^{cr} : crack shear stress
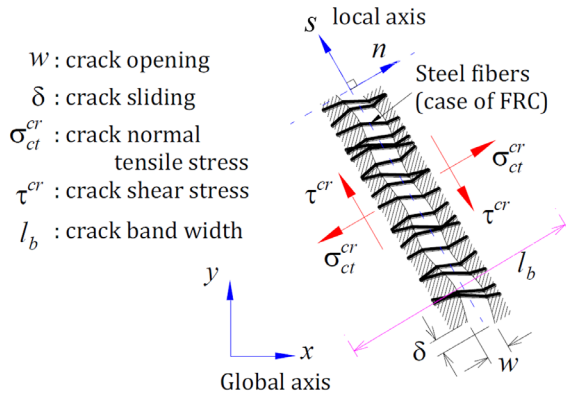l_b : crack band width

Figure 2: Deformation and stress components in the local coordinate system of crack in FRC.

For simulating these two fracture modes, the NLMM104 nonlinear material model of FEMIX was used, whose corresponding diagrams are shown in Figure 3, where G_{fI} and G_{fII} are the fracture energy mode I and II, respectively. In attempt to preserve the results independent of the refinement of the finite element, the crack with and crack sliding are divided by the crack bandwidth, l_b, which is a certain length associated to the geometry of the FE. In the present version, the same l_b was adopted for the crack opening and sliding process. In the NLMM104 model it is assumed that the concrete in compression is in linear elastic behavior, which is an acceptable assumption since the maximum compressive strain level is expected to be much smaller than the SFRC crushing strain.
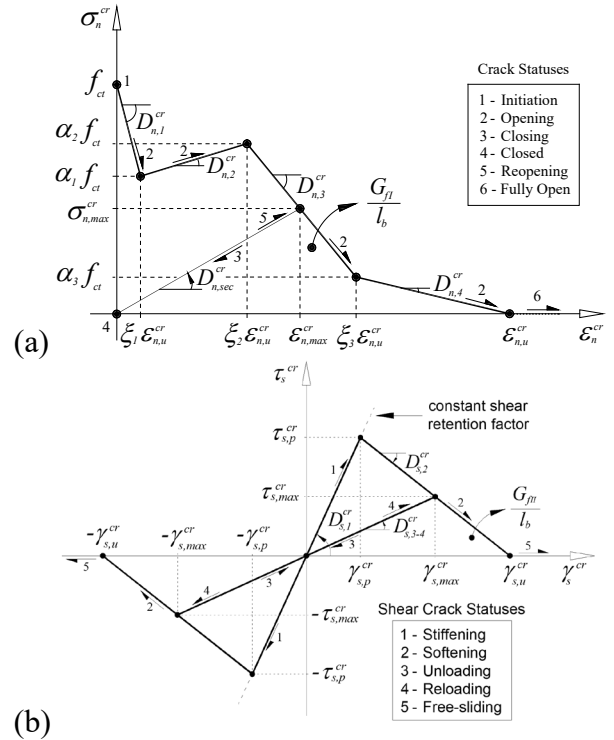
Figure 3: Diagrams for simulating the fracture modes: a) I, and b) II.

The NLMM104 also allows to determine D_s^{cr} according to the concept of shear factor (β):

$$D_s^{cr} = \frac{\beta}{1-\beta} G_c \tag{2}$$

where β can be a constant value ( ]0,1[ ), or defined by an equation that simulates the decrease of β with the increase of the tensile strain to the crack (ε_n^{cr}), such is the following one:

$$\beta = \left(1 - \frac{\varepsilon_n^{cr}}{\varepsilon_{n,u}^{cr}} \right)^{p_1} \tag{3}$$

5

where p_1 determines this decrease rate, in an attempt of reflecting the degradation of the aggregate shear resisting mechanism with the crack opening process. In Eq. (2) G_c is the transverse modulus of elasticity of concrete.

When a crack is completely open ($\varepsilon_n^{cr} \geq \varepsilon_{n,u}^{cr}$, Figure 3), shear stresses cannot be transferred between both faces of the crack, while full interlock is generally assumed for the crack when it closes (*i.e.* $\varepsilon_n^{cr} = 0$). The $\sigma_{n,1}^{cr} = f_t$, the α_i and ξ_i parameters, the G_{fI}, and the l_b define the diagram that simulates the fracture mode I crack propagation. The shear softening diagram that simulates the fracture mode II crack propagation is defined by crack shear strength, $\tau_{s,p}^{cr}$, and G_{fII}, l_b and β (for the pre-peak branch, $D_{s,1}^{cr} = \beta/(1-\beta)G_c$).

The stress-crack opening relationship of FRC was obtained through inverse analysis (IA) [30], using the force-CMOD response from each series of notched beam bending tests with the SFRSCC used in the tested I shape beams. The crack tensile stress versus crack width for these beams is depicted in Figure 4. For numerical simulations, the properties of the first series specimens (150×150×600mm) were assigned to the top and bottom flange, while the properties of the second series (70×70×600mm) were assigned to the web. The average fracture energy from the standard notched beam bending tests is twice as high as the average for the second series. This difference is due to the significant impact of factors like fiber distribution, fiber orientation, and fiber density on fracture energy when analyzing smaller fracture surfaces.
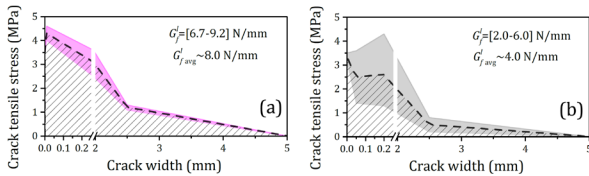

Figure 4: Post-cracking behavior of HPFRC from the back analysis of: (a) first series, and (b) second series of notched beam bending specimens (adapted from [30])

The values of the parameters of the concrete constitutive model adopted in this study are presented in Table 4. The values of the fracture mode II parameters were estimated based on previous research on pure shear of FRC materials [22], but further research in this

domain is required for more reliable estimation of this data.

Table 4: Values of the parameters of the FRC constitutive model (see also Figure 3)

Property	Value
v_c	0.20
E_c (GPa)	35400
f_{cm} (MPa)	73.13
Average tension-softening diagram (Flange)	f_t = 3.5 MPa; G_{fI} = 9.38 N/mm $\xi_1 = 0.0013$; $\alpha_1 = 1.23$; $\xi_2 = 0.091$; $\alpha_2 = 0.89$; $\xi_3 = 0.33$; $\alpha_3 = 0.34$
Average tension-softening diagram (Web)	f_t = 3.0 MPa; G_{fI} = 5.28 N/mm $\xi_1 = 0.007$; $\alpha_1 = 0.73$; $\xi_2 = 0.03$; $\alpha_2 = 0.87$; $\xi_3 = 0.32$; $\alpha_3 = 0.17$
p_1	3
Crack shear softening diagram	$\tau_{s,p}^{cr}$ =1.0 MPa; G_{fII} =2.0 N/mm; β =0.35
l_b	$\sqrt{A_{IP}}$
α_{th} (degrees)	30°
N_{max}^{cr}	2

3.1.2 Simulation of reinforcements

The GFRP bar is assumed to exhibit a linear elastic tensile behavior until failure with a modulus of elasticity, E_f, of 60 GPa, while the steel strand is modeled with an elastoplastic behavior. Figure 5 illustrates the stress-strain relationships for steel strands, and their defining values are included in the caption of this figure.
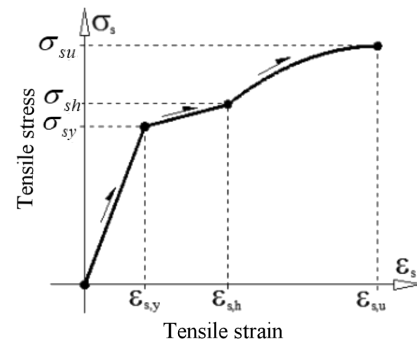

Figure 5: Stress-strain diagram to simulate the behavior of the steel strand (σ_{sy} =1600 MPa, σ_{sh} = 1850 MPa, σ_{su} = 1917 MPa, ε_{sy} =0.1 %, ε_{sh} =4.8 %, ε_{su} =4.8 %).

3.1.3 Simulation of the reinforcement-FRC bond conditions

When bond behavior between the reinforcing bars and FRC is simulated, line interface finite elements were used. The constitutive law for this interface is defined by the bond shear stress versus slip ($\tau - \delta$) diagram shown in Figure 6, whose defining values are included in Table 5. These values were determined through IA using the experimental data from the pullout bending tests conducted by Mazaheripour et al. [27].
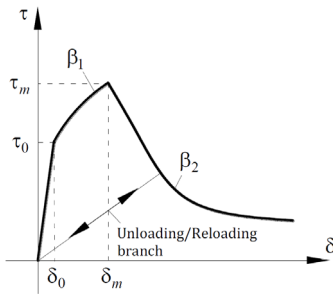

Figure 6: Bond shear stress versus slip diagram.

Table 5 Values defining the bond-slip diagram.

Parameter	GFRP bars	Steel strand
τ_0 (MPa)	11.1	7.8
τ_m (MPa)	21.5	18.1
δ_0 (mm)	0.12	0.09
δ_m (mm)	0.62	0.72
β_1 (-)	0.4	0.4
β_2 (-)	0.4	0.4
K_n (N/mm)*	10^6	10^6

* Stiffness in opening direction of interface FE

3.2 Numerical simulations

The prestress in the reinforcements (considering initial prestress losses indicated in section 2) was applied through uniform temperature variation in the 2D cable FE simulating the flexural reinforcements.

3.2.1 Influence of the refinement of the finite element mesh

Three levels of finite element mesh refinement were utilized to investigate their impact on the simulations of the tested beams. Due to the symmetrical conditions, only one half of the I-beam is simulated. This involved

using finite elements of rectangular shape and dimensions of 25×20 mm², 50×40 mm², and 100×70 mm² (width $\times$ height). The FE meshes for IB5 can be seen in Figure 7. For modeling the FRC material, plain stress Lagrangian 4-node finite elements with 3×2 Gauss-Legendre integration points were utilized. 2D-cable-type finite elements with a 3 Gauss-Legendre integration points (one degree of freedom per node) were employed to simulate the steel and GFRP reinforcements in all simulations. In the simulations where the influence of sliding between the GFRP and surrounding concrete was investigated, linear 4-node interface finite elements were employed with 3 Gauss-Lobatto IP. Elements with continuous variable thickness in their nodes were used in the transition zones between the flanges and web of the beams to correctly simulate the geometry of these zones.
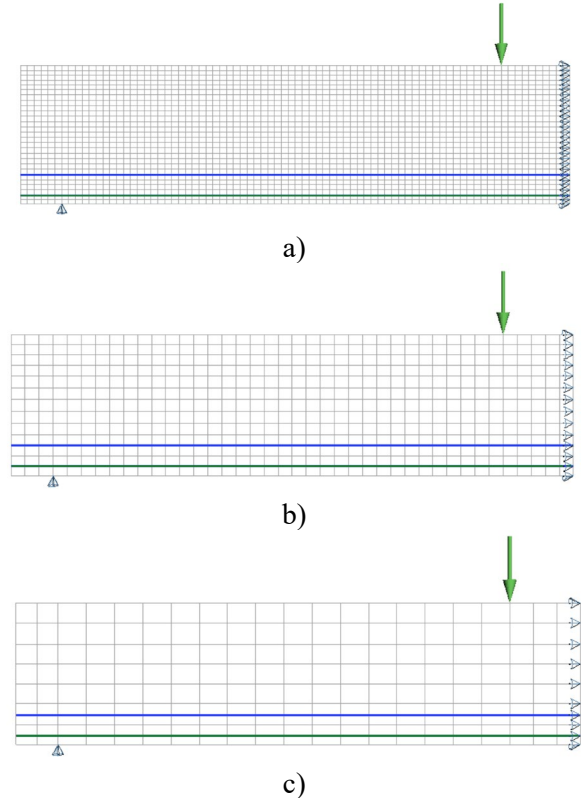

a)

b)

c)

Figure 7: Mesh refinements adopted in the numerical simulations of experimentally tested beams by using finite elements of size: a) 25×20 mm²; b) 50×40 mm²; and c) 100×70 mm² (width $\times$ height). Steel strand: blue line, GFRP bars: green line.

Figure 8 shows the influence of the FE mesh refinement on the force vs mid span deflection ($F\text{-}\delta_c$) of beam IB5, but similar

tendency was observed in the remaining beams. It is verified a small tendency for an increase of the stiffness of the beams in the elasto-cracked stage with the increase of the size of the finite elements, which was already observed in elements failing in shear [15]. However, below a FE size of minimum dimension of 40 mm (almost three times the maximum dimension of aggregates) the results are quite close. Figure 9 shows the numerical crack patterns at the last converged load combination, but only those with a crack width larger than 0.1mm are presented.
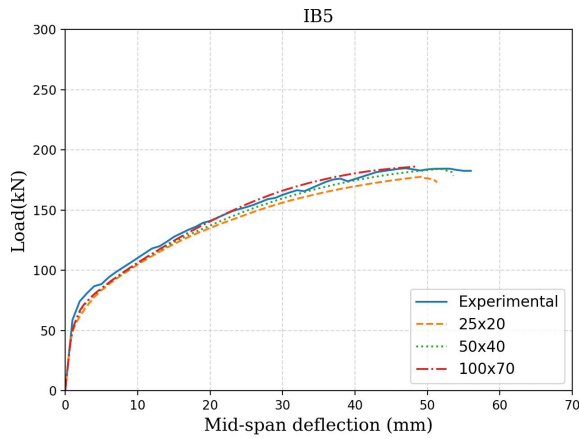
Figure 8: Effect of the mesh refinement on the force-deflection response of the IB5
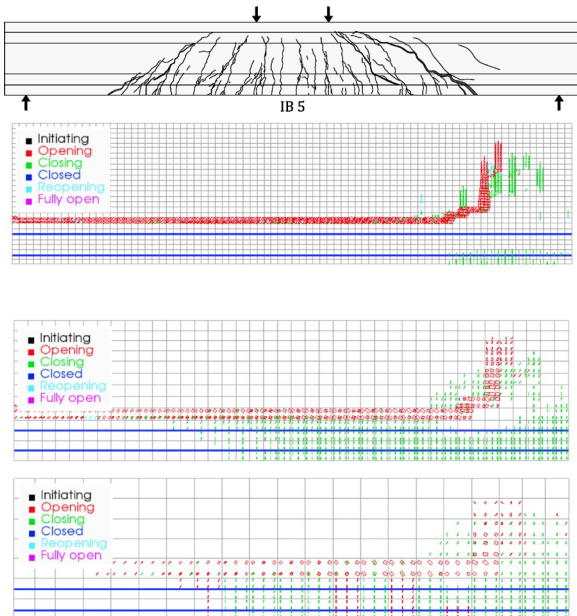
Figure 9: Effect of finite element mesh refinement on the crack patterns of beam IB5

The model, regardless of the FE mesh refinement, suggests the failure be formed by a flexural-shear crack, with the shear crack

progressing horizontally at the bottom of the beam's web, which does not resemble integrally what was observed experimentally. In these simulations, the high possibility of having fibers in the web not effective in loading shear configurations, as demonstrated elsewhere [28, 29], was not considered.

Based on these results, hereafter simulations will be executed with the FE mesh refinement corresponding to FE of $50{\times}40$ mm^2.

3.2.2 Influence of bond conditions

By using line IFEs for modeling an eventual sliding between the flexural reinforcements and surrounding concrete, according to the constitutive law shown in Figure 6 and with the values indicated in Table 5 for defining the parameters of constitutive law of the IFEs, the IB6 were simulated by considering debonding (IFE) and perfect bond (PB) conditions. The F-δ_c registered experimentally and obtained numerically are compared in Figure 10 for these two bond conditions, where it can be concluded that almost null sliding has occurred up to the failure of these beams.
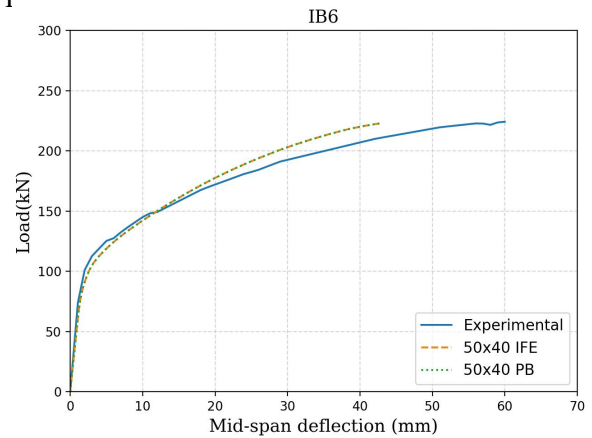

Figure 10: Effect of bond conditions on the force–deflection response of tested beamIB6

3.2.3 Isotropic fracture mode I parameters

Figure 11 presents the F-δ_c curves obtained by using the average diagram represented in Figure 4 through a dashed line. In all simulations, the same mode II fracture parameters were adopted (Table 4). In the case of beam IB5, there is a notable agreement between the experimental and numerical results. However, for the remaining beams, the

numerical simulations slightly overestimate the F-δ_c. This observation confirms that when simulating FRC structures, the assumption of isotropic behavior for post-cracking is debatable. The behavior of FRC strongly relies on factors such as fiber distribution and orientation, making it necessary to consider these aspects in simulations.
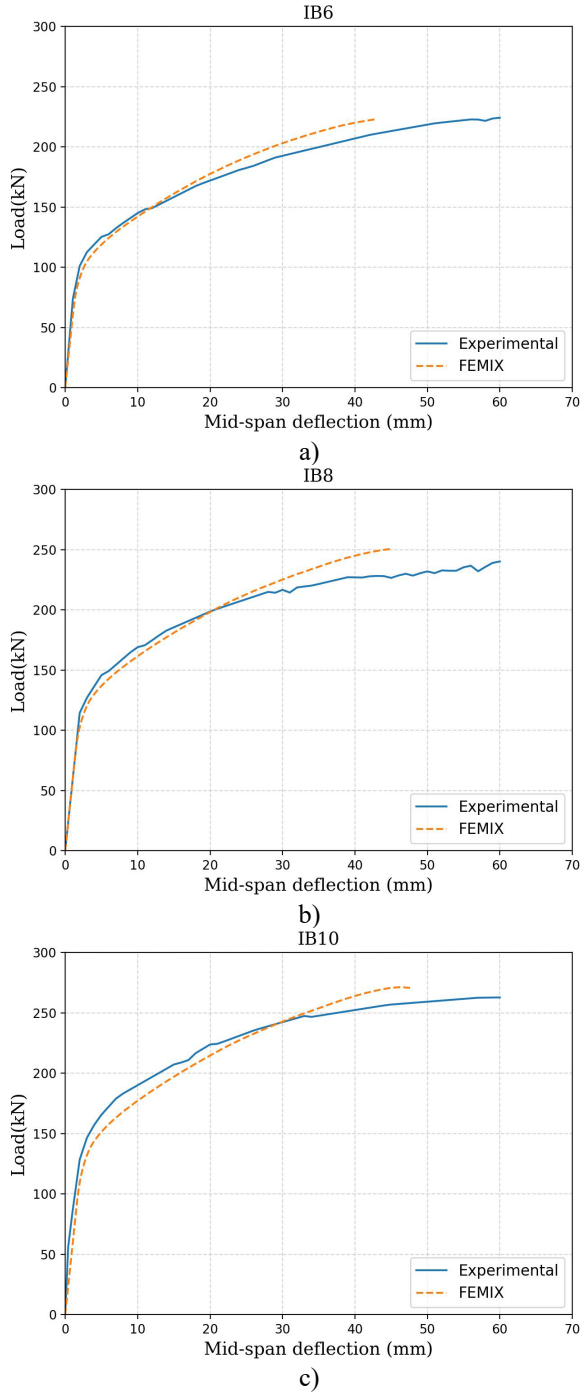

a)

b)

c)

Figure 11: Experimental vs numerical load-deflection of beams: a) IB6; b) IB8; c) IB10

3.2.4 Non-isotropic fracture mode I parameters

Figure 4 has shown the FRC from the web had a much larger dispersion in terms of its post-cracking tensile capacity than the FRC from the flanges. By adopting all possible combinations for the envelope and average post-cracking tensile diagrams of the FRC of these two zones of the beam, each corresponding F-δ_c was obtained numerically (the remaining properties of the constitutive model were maintained the same), and the results are presented in Figure 12. It is verified that considering the lower bounds of the envelope, a significant reduction of the maximum load and its corresponding deflection is predicted. To quantify this variation, the $\left(F^{num} - F^{exp}\right)\big/F^{exp} - \delta_c$ is evaluated for each simulation, where F^{num} and F^{exp} are the forces registered numerically and experimentally for a certain central deflection. The envelop for this relationship is shown in Figure 13, where it is verified that the $\left|\left(F^{num} - F^{exp}\right)\big/F^{exp}\right|$ increases with δ_c, having exceeded 15%.
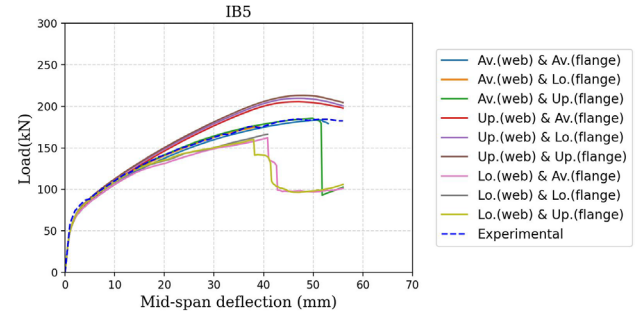

Figure 12: Influence of the dispersion of fracture mode I parameters on the force-deflection
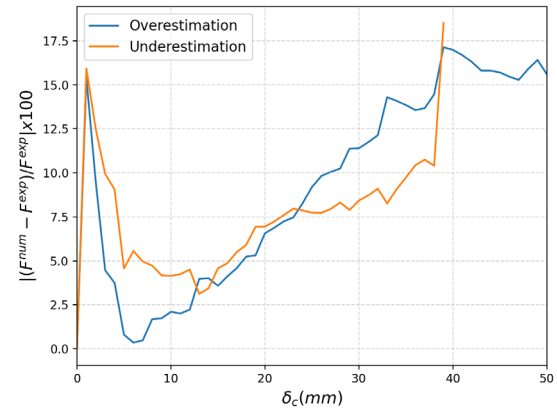

Figure 13: Evolution of the envelop deviation from the experimental force-deflection.

9

3.2.5 Shear retention vs crack shear softening diagram

Two distinct simulations are executed where the unique difference is the approach for simulating the crack shear stress transfer. In one approach was used the concept of shear retention factor introduced in Eqs. (2) and (3), and the other is based on the crack shear softening diagram show in Figure 3b, with the values indicated in Table 4. Figure 14 shows that using the concept of shear retention it is estimated a much larger load carrying capacity than using a crack shear softening diagram. A flexural failure mode is estimated when modeling the crack shear stress transfer with the shear retention factor.
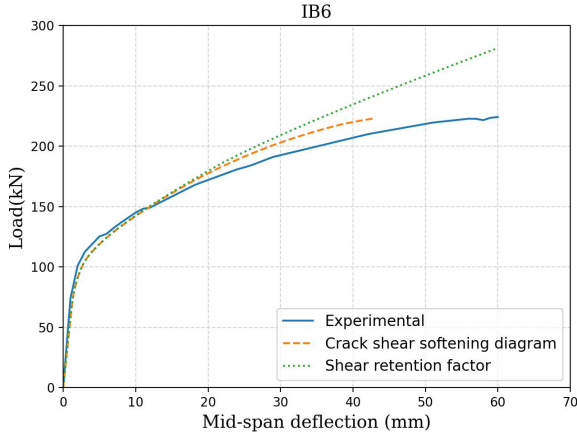

Figure 14: Influence of the approach for simulating the crack shear stress transfer on the load-deflection response in the beam IB6.

3.2.6 Influence of mode II facture energy parameters

A parametric study is conducted with beam IB6 to examine the impact of the parameters defining the crack shear softening diagram on the F-δ_c. The parameters include β, which determines the initial slope of the shear softening diagram (Figure 3b), the crack shear strength ($\tau_{s,p}^{cr}$); and the mode II fracture energy (G_{fII}). The results of these simulations are presented in Figure 15, where it is visible that: no significant impact was observed when varying the value of β (from 0.07 to 0.75); by increasing $\tau_{s,p}^{cr}$ from 0.5 to 2 MPa has increased significantly the load carrying capacity of the beam; the increase of G_{fI} from 1 to 4 N/mm²
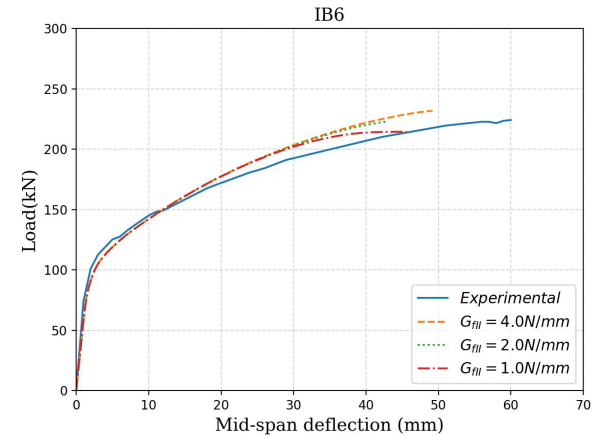
has conducted to an increase of the beam's load carrying capacity, but not so significant like the one registered with $\tau_{s,p}^{cr}$.
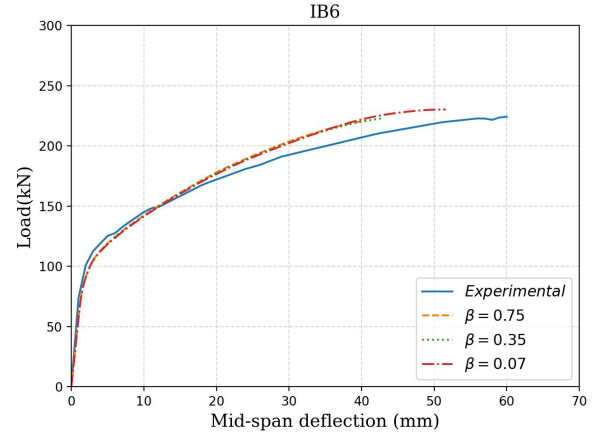
a)
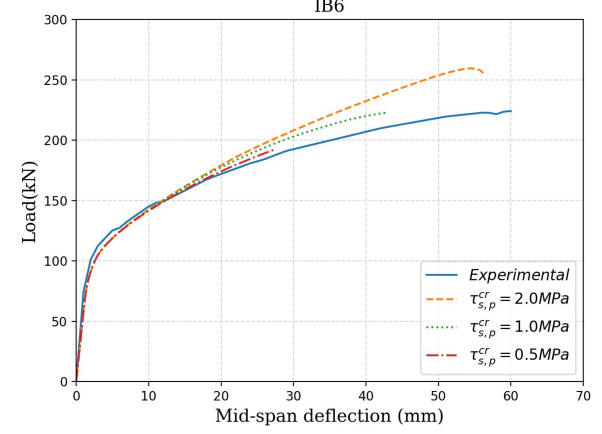
b)

c)

Figure 15: Influence of: a) β, b) $\tau_{s,p}^{cr}$, c) G_{fII}.

4 CONCLUSIONS

The present study investigated the capabilities and limitations of a multi-directional fixed smeared crack model (MDFSCM) in predicting the behavior of

hybrid prestressed GFRP-steel reinforced concrete beams subjected to shear failure. Four experimentally tested beams were simulated numerically, and the following conclusions can be drawn based on the simulation results:

- The MSDFSCM demonstrated capable of assuring good predictions, regardless the finite element mesh refinement, as long as the dimension of the finite elements are smaller or equal to three times the maximum dimension of the aggregates;

- Beams failing in shear, such was the case of the experimentally tested ones, assuming perfect bond conditions for the flexural reinforcements is a correct assumption, since debonding is marginal up to the failure of these beams;

- Adopting the concept of shear retention factor to simulate the crack shear stress transfer provides unsafe predictions and a more ductile failure mode than observed experimentally. By simulating the crack shear stress transfer with a crack shear softening diagram, a good estimative of the force-deflection relation and failure mode was obtained.

- The variation of the fracture mode I parameters has a significant impact on the predictive performance of the model, with force deviation error that attained a value close to 15%. Using global resistance methods is recommended to the design of this type of structures.

- Amongst the parameters that define the crack shear softening diagram, the crack shear strength is the one with the highest impact on the predictive performance of the model, by increasing the beam's load carrying capacity with the value of $\tau_{s,p}^{cr}$.

Regarding the efficiency of the hybrid flexural reinforcement applied with a certain prestress level, together with the use of short fibers as a shear reinforcement, it was verified that, despite a shear crack was formed at the failure of these beams, this occurred at a deflection much higher than the deflection limit for the SLS verifications, therefore this concept allows this type of beams to have a relatively high deformability up to their failure.

Reference

1. Zhang, P., et al., *A review on fracture properties of steel fiber reinforced concrete.* Journal of Building Engineering, 2023: p. 105975.

2. Ahmad, J., et al., *A study on mechanical and durability aspects of concrete modified with steel fibers (SFs).* Civ. Eng. Archit, 2020. **8**: p. 814-823.

3. Feng, G., et al., *A review on mechanical properties and deterioration mechanisms of FRP bars under severe environmental and loading conditions.* Cement and Concrete Composites, 2022: p. 104758.

4. Goldston, M., A. Remennikov, and M.N. Sheikh, *Experimental investigation of the behaviour of concrete beams reinforced with GFRP bars under static and impact loading.* Engineering Structures, 2016. **113**: p. 220-232.

5. Ashour, A., *Flexural and shear capacities of concrete beams reinforced with GFRP bars.* Construction and Building Materials, 2006. **20**(10): p. 1005-1015.

6. Hajiloo, H., et al., *GFRP-reinforced concrete slabs: Fire resistance and design efficiency.* Journal of Composites for Construction, 2019. **23**(2): p. 04019009.

7. Abadel, A., et al., *Shear behavior of self-consolidating concrete deep beams reinforced with hybrid of steel and GFRP bars.* Ain Shams Engineering Journal, 2023: p. 102136.

8. Yost, J.R., S.P. Gross, and D.W. Dinehart, *Shear strength of normal strength concrete beams reinforced with deformed GFRP bars.* Journal of composites for construction, 2001. **5**(4): p. 268-275.

9.   Kaszubska, M., et al., *Shear behavior of concrete beams reinforced exclusively with longitudinal glass fiber reinforced polymer bars: Experimental research.* Structural Concrete, 2018. **19**(1): p. 152-161.

10.   Le, T.D., et al., *Performance of precast segmental concrete beams posttensioned with carbon fiber-reinforced polymer (CFRP) tendons.* Composite Structures, 2019. **208**: p. 56-69.

11.   Hussein, L.F., M.M. Khattab, and M.S. Farman, *Experimental and finite element studies on the behavior of hybrid reinforced concrete beams.* Case Studies in Construction Materials, 2021. **15**: p. e00607.

12.   ELWakkad, N.Y., et al., *Experimental Study and Finite Element Modelling of the Torsional Behavior of Self-Compacting Reinforced Concrete (SCRC) Beams Strengthened by GFRP.* Case Studies in Construction Materials, 2023: p. e02123.

13.   Mustafa, S.A. and H.A. Hassan, *Behavior of concrete beams reinforced with hybrid steel and FRP composites.* HBRC journal, 2018. **14**(3): p. 300-308.

14.   Soltanzadeh, F., et al., *Effect of fiber dosage and prestress level on shear behavior of hybrid GFRP-steel reinforced concrete I-shape beams without stirrups.* Composites Part B: Engineering, 2016. **102**: p. 57-77.

15.   Barros, J.A., H. Baghi, and A. Ventura-Gouveia, *Assessing the applicability of a smeared crack approach for simulating the behaviour of concrete beams flexurally reinforced with GFRP bars and failing in shear.* Engineering Structures, 2021. **227**: p. 111391.

16.   Barros, J., et al., *Blind competition on the numerical simulation of continuous shallow steel-fiber reinforced concrete beams failing in bending.* Structural Concrete, 2023.

17.   Barros, J., et al., *Blind competition on the numerical simulation of steel-fiber-reinforced concrete beams failing in shear.* Structural Concrete, 2021. **22**(2): p. 939-967.

18.   Breveglieri, M., et al., *Strategies for numerical modeling the behavior of RC beams strengthened in shear using the ETS technique.* Engineering Structures, 2016. **128**: p. 296-315.

19.   Zhang, X. and D. Wang. *Influence of the shear retention factor on the fracture behavior of fiber reinforced concrete.* in *Advances in Materials Sciences, Energy Technology and Environmental Engineering: Proceedings of the International Conference on Materials Science, Energy Technology and Environmental Engineering, MSETEE 2016, Zhuhai, China, May 28-29, 2016.* 2017. CRC Press.

20.   Gouveia, A.V., et al., *Multi-fixed smeared 3D crack model to simulate the behavior of fiber reinforced concrete structures.* 2008.

21.   Mazaheripour, H., et al., *Deflection and cracking behavior of SFRSCC beams reinforced with hybrid prestressed GFRP and steel reinforcements.* Engineering Structures, 2016. **125**: p. 546-565.

22.   Soltanzadeh, F., J.A. Barros, and R. Santos, *High performance fiber reinforced concrete for the shear reinforcement: Experimental and numerical research.* Construction and Building Materials, 2015. **77**: p. 94-109.

23.   Standard, A., *Standard test method for static modulus of elasticity and poisson's ratio of concrete in compression.* ASTM Stand. C, 2010. **469**.

24.   Matos, L.M., et al., *A new inverse analysis approach for predicting the fracture mode I parameters of fibre reinforced concrete.* Engineering Fracture Mechanics, 2021. **246**: p. 107613.

25.   CEN, *Test method for metallic fibre concrete - Measuring the flexural tensile strength (limit of proportionality (LOP), residual)*, A, Editor. 2005, CEN: Brussels. p. 17.

26.   Ventura-Gouveia, A., *Constitutive models for the material nonlinear analysis of concrete structures including time dependent effects.* Department of Civil Engineering, PhD Thesis, 2011.

27.   Mazaheripour, H., et al., *Experimental and theoretical study on bond behavior of GFRP bars in steel fiber reinforced self compacting concrete.* 2012.

28.   Lee, G.G. and S.J. Foster, *Behaviour of steel fibre reinforced mortar in shear 1: Direct shear testing.* Sydney: Univ. of New South Wales, 2006. **Report No.: R-444**.

29.   Lee, G.G. and S.J. Foster, *Behaviour of steel fibre reinforced mortar in shear 2: Gamma ray imaging.* Sydney: Univ. of New South Wales, 2006. **Report No.: R-445**.

30.   Mazaheripour, H., *Structural behavior of hybrid GFRP and steel reinforced FRC prestressed beams.* 2015, Universidade do Minho (Portugal).